Energy & Environmental Science

ROYAL SOCIETY OF CHEMISTRY

PAPER

View Article Online
View Journal | View Issue

Cite this: *Energy Environ. Sci.*, 2025, **18**, 10180

Resting but not idle: unveiling the mechanistic origin of resting losses for zinc anodes

John F. Koons, †[a] Ashutosh Rana, †[a] Md. Arif Faisal, †[a] James H. Nguyen, [a] Saptarshi Paul,[a] Jeremy H. Lawrence [a] and Jeffrey E. Dick *[ab]

Resting losses in aqueous zinc metal batteries (AZMBs) can exceed over 15% of anode capacity within hours; severe enough to cripple grid-scale deployment. These losses are reported to occur regardless of electrolyte ($ZnSO_4$, $Zn(OTf)_2$, $ZnCl_2$), current collector (Cu, Ti, Ni, C, stainless steel, Pt), temperature, or other conditions. This is widely attributed to the thermodynamic advantage of the hydrogen evolution reaction (HER, 0 V *vs.* SHE) over Zn/Zn^{2+} (−0.76 V *vs.* SHE), driving rapid dissolution of plated Zn on the current collector with spontaneous H_2 release. By contrast, analogous non-aqueous Li and Na systems show only a fraction of such losses, highlighting corrosion mechanisms unique to Zn. Understanding the mechanistic origins of capacity fading under resting conditions remains a major barrier and must be addressed to establish the design principles needed to mitigate high resting losses in AZMBs. In this work, we use fluorescence microscopy to reveal lateral propagation of cathodic current across current collectors, showing that spontaneous electron exchange occurs not only on deposited Zn but also on the current collector itself, substantially accelerating corrosion. Applying mixed potential theory, we show that electron transfer kinetics, thermodynamic reduction potentials, and concentration polarization collectively govern corrosion rates. We apply *in situ operando* electrochemical mass spectrometry to precisely quantify resting corrosion rates and faradaic efficiencies, and our results clearly show that these rates vary by several orders of magnitude depending on the HER kinetics of the current collector. Mechanistically, our results show that galvanic corrosion extends beyond just the anode active materials, to the current collector and other coin cell components, including casings, spacers, and springs; whose catalytic activity toward HER exacerbates irreversible consumption of active Zn. We show that these hidden corrosion pathways operate under both resting and cycling conditions, explaining paradoxical HER observations during Zn stripping. By systematically linking deposited Zn, current collectors, and non-electrode components, this study unifies prior observations of resting corrosion, provides a mechanistic understanding of capacity fading origins, and establishes design principles to mitigate losses.

Received 27th August 2025,
Accepted 8th October 2025

DOI: 10.1039/d5ee05063d

rsc.li/ees

Broader context

Grid-level energy storage is an issue of ever-increasing importance in today's society as we move toward green energy solutions to the rapidly growing energy demands of the modern world. Aqueous zinc metal batteries (AZMBs) stand out as promising battery candidates for this role given their relative safety and cheap cost compared to other modern batteries like Li-ion. Despite this, recent work has shown that AZMBs also suffer from far higher levels of corrosion than other batteries leading to loss of charge while resting, representing a major roadblock in using them for grid-level energy storage. While several observations have been made of this process, to date, there is no all-encompassing detailed mechanistic model that accounts for factors beyond zinc, like how battery materials such as the current collector affect corrosion. This work bridges that gap to definitively show how materials such as the current collector or a coin cell case can drastically change the corrosion process. In doing so, we provide a clear way to accurately predict corrosion in AZMBs and allow for the development of targeted an effective mitigation strategies, opening the path for the development of robust AZMBs that can effectively store energy on a grid-level.

Introduction

Aqueous zinc metal batteries (AZMBs) are promising candidates for grid level energy storage – offering several advantages including high theoretical capacity (820 mAh g^{-1}), use of

[a] *Department of Chemistry, Purdue University, IN, USA. E-mail: jdick@purdue.edu*
[b] *Department of Electrical and Computer Engineering, Purdue University, IN, USA*
† These authors contributed equally to this work.

aqueous electrolytes, good inherent safety, and affordability of materials.[1–5] In recent years, extensive research on cathode, anode, electrolyte, and solid electrolyte interface (SEI) engineering has led to significant improvements in the cyclability of AZMBs.[6–9] Specifically, research on Zn metal anodes has focused on the use of novel electrolyte formulations, additives or anode materials to suppress commonly observed issues like dendritic growth of Zn, formation of non-uniform or unstable corrosion layers and the hydrogen evolution reaction (HER).[10–17] Several works have also developed specific battery cycling protocols to plate and strip Zn in a manner that effectively addresses these issues.[18–21] These collective efforts have led to remarkable improvements in the cycling stability of anodes, as well as in the overall performance of AZMBs.

It is readily apparent that majority of studies primarily focus on the direct optimization of electrode components, namely, the two working electrodes (anode + cathode), separator, and electrolyte. In contrast, non-electrode components (like spacer, spring, casing) have received comparatively less attention, despite evidence showing that they can be equally important determining in battery performance.[22,23] Consequently, coin cells and pouch cells largely remain a ''black box'' mechanistically while cycling, and recent studies have highlighted that relying solely on electrochemical data can lead to misinterpretation of battery cycling stability.[13,24] Additionally, most improvements in AZMB anode cycling stability have focused on galvanostatically driven reactions (Zn plating during charging and Zn stripping during discharging). This focus has overshadowed an equally critical aspect of anode stability: behavior under resting conditions, when the battery is left *idle*.[25–29] While well recognized in non-aqueous Li and Na battery systems, this phenomenon remains largely unexplored in AZMBs.[30–35] This is of utmost importance for AZMBs, particularly in practical use cases such as grid storage, where batteries may remain idle for prolonged periods.

For AZMB anodes, the battery is never truly idle under resting conditions, as spontaneous redox reactions are continuously driven by thermodynamic forces. The primary reaction of interest is the tendency of Zn deposited on the current collector to oxidize while simultaneously generating H_2 through H^+ reduction in typical mildly acidic Zn electrolytes (pH 4–6).[36–38] This occurs due to the thermodynamic advantage of the hydrogen evolution reaction (HER) (0 V *vs.* SHE) relative to the Zn/Zn^{2+} redox couple (−0.76 V *vs.* SHE), leading to a spontaneous electron exchange and, consequently, loss of the Zn inventory/capacity. This drives the self-discharge behavior of Zn batteries, where loss of Zn capacity reduces the state of charge. This aspect has recently been explored in literature and has been shown to deserve more attention, as several groups have observed significant loss of Zn capacity at the anode after relatively short periods of resting.[39–42] These capacity losses are quantified using coulombic efficiency (% CE), defined as the percentage of plated Zn that can be electrochemically stripped from the current collector after prolonged resting periods. % CE losses of well over 15% have been reported in Zn coin cells and pouch cells after resting for several hours.[41] Such significant resting losses at the anode are a unique feature of Zn systems, in contrast to Li-ion or Li-metal batteries, where corresponding losses are much lower.[32,34] However, a detailed mechanistic understanding of the process behind resting Zn inventory loss is missing. It is crucial to mention that these substantial losses have been reported regardless of the choice of electrolyte ($ZnSO_4$, $Zn(OTf)_2$, $ZnCl_2$) or current collector (Cu, Ti, Ni, C, stainless steel (SS), Pt, *etc.*), temperature, and other conditions.[39,42] Most importantly, this loss occurs spontaneously, without any applied current or voltage, that is, under open-circuit conditions. This highlights a critical, yet often overlooked, bottleneck in AZMBs beyond the well-known cathode and anode limitations. Understanding the mechanistic details of these spontaneous redox reactions that occur during rest is essential to explain these Zn losses.

It is well recognized that under resting/open circuit conditions, metallic Zn will react with H^+ or H_2O in mildly acidic electrolytes to form H_2, and zinc hydroxide, $Zn(OH)_2$, which will further react with electrolyte counter anions in solution to form an SEI. For example, in $ZnSO_4$ electrolyte, metallic zinc will form zinc hydroxide sulfate, $ZnSO_4[Zn(OH)_4]_3{\cdot}xH_2O$ (ZHS) through the reactions shown in eqn (1) and (2).[12,43–45]

$$Zn + 2H_2O \rightarrow Zn(OH)_2 + H_2 \quad (1)$$

$$ZnSO_4{\cdot}xH_2O + 3Zn(OH)_2 \rightarrow ZnSO_4[Zn(OH)_2]_3{\cdot}xH_2O \quad (2)$$

Current understanding of Zn resting capacity loss concludes that it originates from spontaneous HER on deposited Zn and proceeds through several potential pathways: (i) H_2 evolution promotes the formation of inactive or ''dead'' zinc *via* detachment from the electrode surface, while SEI formation irreversibly consumes active Zn ions, (ii) nucleation of H_2 bubbles can electrically isolate deposited zinc on the current collector, and (iii) the dissolution of plated Zn through galvanic oxidation during HER. Although these mechanisms differ, they all result in permanent loss of reversible Zn capacity during resting periods. These works demonstrated that the magnitude of loss due to Zn corrosion is directly related to the electrolyte pH, reducing with the addition of buffering agents, and varies significantly with the current collector material.[39,41,42] Consequently, several methods have been proposed to mitigate resting corrosion losses, including reducing electrolyte acidity, degassing coin cells, and engineering current collectors that inhibit Zn corrosion and detachment. While these efforts show promise, they do not provide a clear understanding of the underlying mechanisms, which is essential for designing targeted mitigation strategies.

This knowledge gap exists because most studies in this emerging field have focused primarily on attributing resting corrosion behavior solely to the deposited Zn eqn (1) and (2). Drawing inspiration from Li systems, factors beyond the active metal itself can significantly contribute to corrosion and resting losses; however, these contributions remain poorly recognized and largely unexplored in the AZMB field.[33] Consequently, significant uncertainty remains not only regarding the role of Zn but also concerning how the surrounding electrolyte, non-electrode components, and current collectors influence the

underlying mechanism. For example, if Zn is plated on a Cu current collector submerged in the same electrolyte, could Cu's higher catalytic activity toward HER, compared to Zn, accelerate spontaneous corrosion and capacity loss? Could this effect be further amplified when other coin cell components such as spacers, casings, and springs made of SS, which are even more catalytically active than Cu and Zn, are present? Understanding these processes is critical yet challenging due to the spatial heterogeneity of competing reactions. Current methods cannot quantitatively track how cathodic currents, such as HER, spread across a current collector in real time. Observing H_2 bubble nucleation provides only qualitative insight and fails to capture the spatial dynamics of heterogeneous electron transfer. Thus, there is a pressing need for techniques that can quantify how corrosion propagates from plated Zn to the current collector, how quickly it occurs, and what factors govern its rate. Understanding these aspects is critical for developing design principles for practically relevant AZMBs. The mechanistic foundation for these questions is presented and demonstrated in this work, revealing a completely new and previously unexplored dimension in the field of AZMBs.

In this work, the corrosion process on Zn metal anodes is critically explored, providing mechanistic insights into the origins of capacity fading under resting conditions. Our work reveals that spontaneous electron exchange occurs not only on Zn plated on conducting current collectors such as Cu, Ti, SS, C, and Pt, but also on the current collectors themselves, significantly influencing corrosion rates and mechanisms due to their distinct HER kinetics. Herein, we employ a range of analytical techniques including H_2 bubble observation, scanning electron microscopy (SEM) with energy-dispersive X-ray spectroscopy (EDX), fluorescence microscopy, and *in situ operando* electrochemical mass spectrometry (ECMS) to gain a comprehensive understanding of the mechanisms driving resting losses in AZMB anodes. We first observe the existence of different corrosion mechanisms based on whether the current collector material can actively participate in driving HER cathodically. We then take a novel systematic approach to image the electron exchange reaction on both the Zn and surrounding conductor for the first time: replacing HER on Zn with the spontaneous reduction of resazurin (RZ) to resorufin (RF), which can be tracked using fluorescent microscopy. This system allows us to track the lateral spread of charge on the current collector and demonstrate its role in Zn corrosion. Using these observations, we apply the system to fundamental mixed potential theory and demonstrate how electron exchange kinetics of conductive surfaces, thermodynamic reduction potentials, and concentration polarization collectively influence the rate of the corrosion reaction. Next, we use ECMS to quantify the resting corrosion rates of several current collector materials in comparison to Zn itself to show that the resting corrosion rate can differ by several orders of magnitude depending on the current collector's HER kinetics. This work establishes a mechanistic foundation for corrosion in AZMB anodes, revealing that galvanic corrosion extends beyond the anode itself to involve coin cell components such as casings, spacers, and springs. We demonstrate that these materials, depending on their catalytic activity toward HER, can exacerbate spontaneous corrosion reactions, accelerating the loss of Zn capacity and battery failure. These hidden corrosion pathways occur not only under resting conditions but also manifest during cycling, providing a mechanistic explanation for surprising and paradoxical observations of HER during Zn stripping. By systematically linking the roles of deposited Zn, current collectors, and non-electrode components, this study unifies prior observations of resting corrosion. It provides a mechanistic understanding of the origins of resting loss and opens new avenues for mitigating losses and improving AZMB performance.

Experimental section

Materials

Granular zinc Zn, 20 mesh, potassium chloride (KCl), zinc sulfate hexahydrate ($ZnSO_4$), and sodium resazurin salt were purchased from Sigma Aldrich (St. Louis, MO). Glass microscope slides were purchased from VWR (Radnor, PA) and indium tin oxide (ITO) microscope slides were purchased from Qunguan (Osaka-Fu, Japan). Ultrapure water (18 MΩ cm^{-1}) was used for all aqueous solutions. CR2032 coin-type cells, Zn foil (∅ 15 mm, 25 μm), Cu foil (∅ 15 mm, 25 μm), Ti foil (∅ 15 mm, 25 μm), and filter paper separator (∅ 19 mm) were purchased from MTI Corporation (Richmond, CA) and used for all coin cells.

Instrumentation

Resazurin experiments were done on a Leica DMi8 microscope (Leica Microsystems, Germany) equipped with a pE-300lite light source (CoolLED, United Kingdom). Fluorescence was taken with the Y3 filter (Leica Microsystems, Germany) that has an excitation of 532–558 nm, a dichroic mirror at 565 nm, and an emission of 570–640 nm. The objective used was 5× with a numerical aperture of 0.12. A complementary metal-oxide semiconductor camera (Orca-Flash4.0 Digital CMOS C13440-20CU from Hamamatsu, Hamamatsu, Japan) was used to capture images. CR2032 coin-type cells were assembled under ambient air conditions and assessed using a Neware battery test system filter paper separator (∅ 19 mm), and 50 μL of electrolyte. Electron microscopy was performed with an Apreo 2s scanning electron microscope from FEI (Hillsboro, OR). EDX was done using an Oxford Aztec Xstream-2 silicon drift detector with Xmax80mm window (Oxford Instruments, High Wycombe, UK). Electrochemical measurements were taken on either a CHI 6284E potentiostat from CH Instruments (Austin, TX) or a BioLogic VSP 300 potentiostat from BioLogic (Willow Hill, PA). ECMS measurements were made using a SpectroInlets ECMS premium model with a Pfeiffer Prisma Pro mass analyzer (Soborg, Denmark). Cu, Zn, glassy carbon, Ti, and stainless-steel disk electrodes from SpectroInlets were used for EC-MS measurements. Glassy carbon inlaid disk electrodes from CH Instruments were used for all other electrochemical measurements.

Coin cell cycling

Ti|Zn and Cu|Zn coin cells used for comparing coulombic efficiency were prepared with 50 μL of 2 M $ZnSO_4$ electrolyte. They were cycled at 1 mA cm^{-2} for a capacity of 1 mAh cm^{-2} with varying resting times between plating and stripping from the Cu or Ti anode. When testing for corrosion on SS coin cell cases, coin cells were filled with 200 μL of 2 M $ZnSO_4$ and cycled at 1 mA cm^{-2} for a capacity of 5 mAh cm^{-2}.

Observation of corrosion on foils

2 M $ZnSO_4$ was prepared. Cu or Ti foils were plated with 50 mA cathodic current for 20 s in 2 M $ZnSO_4$ solution. Foils were washed with ultrapure water. Foils were then placed in a Petri dish and submerged in 2 M $ZnSO_4$ electrolyte. Corrosion was recorded using a phone camera. Following corrosion, foils were washed with ultrapure water and sputtered with a Pt sputter coater before SEM/EDX analysis. For the case where Cu and Ti foils rested for 6 h, they were placed in a test tube and submerged in 2 M $ZnSO_4$, which was covered with parafilm to prevent evaporation. When observing corrosion on SS coin cell cases, Zn was plated on Cu foil in the same manner and placed inside of the case. The foil was held in contact with the case and 2 M $ZnSO_4$ was pipetted in to fill the case. Both the case and the Cu foil were sputter coated in the same manner with Pt prior to SEM/EDX analysis.

Resazurin reduction

A 1 mM resazurin solution was prepared and the pH was adjusted to 4.0 using HCl. Granular Zn (6 mg) was measured and placed on either a glass slide or ITO slide and placed on the microscope stage. A pipette was used to drop resazurin solution (50 μL, 1 mM, pH 4) on top of the particles. The reaction was captured with 50 ms exposure on and the Y3 filter cube. The captured video was processed using Fiji open software. Contrast was set at the same values for all frames that were analyzed for their intensity. The hot-magma lookup table was applied to the videos. This process was repeated with a 50× diluted resazurin solution (50 μM). In this case the exposure time was increased to 250 ms and the videos were processed in the same manner.

Electrochemical mass spectrometry

Previous work has used ECMS to capture and quantify the gas evolved during electrodeposition and stripping of Zn on various electrodes. In this case, Argon carrier gas was used at a flow rate of 1 mL min^{-1} to capture volatile species through the membrane chip of the ECMS electrochemical cell. EC-Lab software was used to control the BioLogic potentiostat and Zilien software was used to control the ECMS instrument. Various working, counter and reference electrode setups were used as outlines in the main manuscript and SI. The ECMS m/z = 2 signal was calibrated for H_2 by an internal production method, which was performed with a polycrystalline platinum disk electrode in 1 M perchloric acid electrolyte. Galvanostatic reductive biases were applied for at least 150 seconds until a steady-state detector current was observed. This steady-state current is plotted against calculated internal H_2 production in Fig. S5. The calculated production of H_2 was determined by using an n = 2 for electrons per hydrogen atom evolved and Faraday's constant, F, to convert from C to mol H_2. The best-fit slope of 0.44 C per mol H_2 was used for all flux calculations.

Results and discussion

Visualization of resting corrosion mechanisms

We first performed % CE tests on Cu|Zn and Ti|Zn asymmetric coin cells in 2 M $ZnSO_4$ with different resting periods between plating Zn on the current collector and stripping back off. The cells were cycled at 1 mA cm^{-2} for a capacity of 1 mAh cm^{-2}. Fig. 1a displays the average % CE values for coin cells with no rest, a 6 h rest and a 24 h rest to be 78.7%, 66.9% and 60.8%, respectively, for Cu|Zn cells and 91.4%, 84.7% and 68.3%, respectively, for Ti|Zn cells. The mean values with standard deviation are reported in Fig. S1. Additionally, these % CE loss values did not appear to follow a significant trend with varying electrolyte volume, showing similar losses at 2 M $ZnSO_4$ volumes ranging from 30 μL to 150 μL (Fig. S2). We then calculated the % CE lost during resting by subtracting the % CE after resting from the zero-rest value. These % CE losses for Cu and Ti current collectors are compared to Cu and SS current collectors from Liu *et al.* (R1) and a Ti current collector from Pu *et al.* (R2) when plated at 1 mA cm^{-2} and rested for 24 h in Fig. 1b.[39,40] While our values of % CE losses are lower than the other reported values, the trend of Ti experiencing a larger resting loss than Cu is consistent. Notably, reported values of resting loss on SS current collectors are higher than those of Cu. While the relation between Cu and SS current collectors can be explained by the comparatively lower onset potential of HER on SS, the higher observed losses on Ti contradict this trend, since the onset potential of HER is more negative on Ti than either Cu or SS (Fig. S3). In addition to this contradiction, several other observations suggest a more nuanced corrosion predictor than simply HER activity of the current collector. First, Cu and Ti have drastically different average % CE's of 78.7% and 91.4%, respectively, without resting. Second, while Cu|Zn coin cells lose most of their % CE in the first 6 h with only slightly further loss at 24 h, Ti|Zn coin cells experience a relatively small loss in the first 6 h, followed by a significantly larger one at 24 h. These observations suggest that there may be different mechanisms of corrosion during resting, warranting further investigation.

We sought to visualize this difference by submerging four different foils – (1) bare Cu foil, (2) Zn plated on Cu foil, (3) Zn plated on Ti foil, and (4) Zn plated on Ti foil with a Cu foil electrically attached – in 2 M $ZnSO_4$, as seen in Fig. 1c. This test allowed us to visualize the progress of corrosion on the plated Zn and the current collectors over time by viewing H_2 bubble formation on the metal surfaces. Fig. 1c displays a snapshot only 1 min after submersion and already shows significant bubbling across the Cu surfaces in foils 2 and 4 (see Video S1).

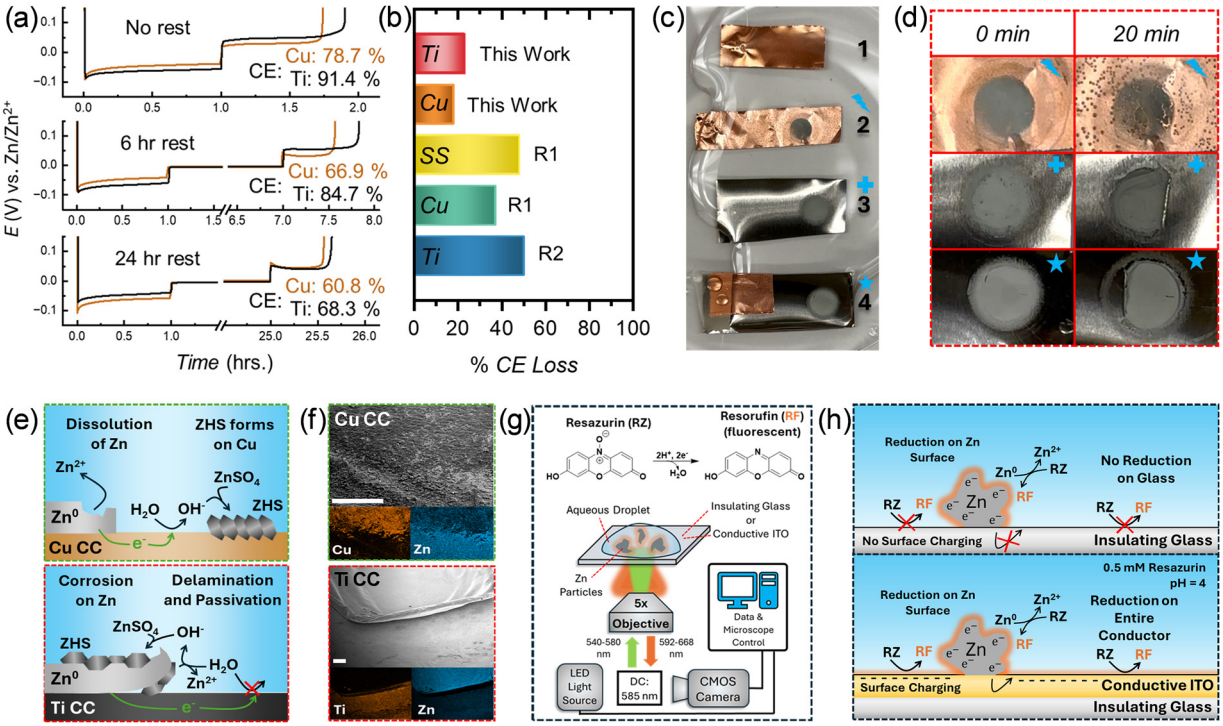

Fig. 1 (a) Average coulombic efficiency (CE) values of Cu|Zn and Ti|Zn asymmetric coin cells with 0 h, 6 h, or 24 h rest between plating and stripping while cycled at 1 mA cm^{-2} and 1 mAh cm^{-2} capacity in 2 M $ZnSO_4$. (b) Reported CE losses after 24 h rest in asymmetric coin cells cycled at 1 mA cm^{-2} in 2 M $ZnSO_4$ with Cu, Ti and stainless-steel (SS) current collectors from this work, R1 and R2. (c) Image of (1) bare Cu foil, (2) Zn plated on Cu foil, (3) Zn plated on Ti foil, and (4) Zn plated on Ti foil with Cu electrically connected submerged in 2 M $ZnSO_4$ after 1 minute. (d) Optical images of Cu foils 2 (lightning), 3 (plus) and 4 (star) showing the evolution of the plated Zn before submersion in 2 M $ZnSO_4$ and after 20 minutes of submersion. (e) Schematic proposing the different corrosion mechanisms of plated Zn on Cu *vs.* Ti current collectors (CC). (f) SEM images and EDX maps of Zn plated on Cu foil (top) or Ti foil (bottom) after soaking in 2 M $ZnSO_4$ for 6 h. Zn was originally plated on the top half of each image. Scale bars are 250 μm. (g) Schematic of the reduction of resazurin (RZ) to fluorescent resorufin (RF) and the microscopy experimental setup used. (h) Schematic displaying the reduction patterns observed when a RZ droplet was placed on Zn particles on either insulating glass or conductive ITO.

In contrast, no bubbling is seen on foils 1 and 3 even after 20 min of submersion. Foil 1 does not react because the oxidation of Cu to reduce H^+ or H_2O is thermodynamically unfavorable under these conditions. The lack of bubbling on foil 3 can be explained by Ti's relatively high overpotential for HER. In both cases that bubble, Cu foil is electrically connected to plated Zn (either directly or through Ti) and submerged in the same electrolyte, allowing for HER to occur on both the Zn and Cu surfaces as Zn oxidizes, producing H_2 gas bubbles. In this way, Cu's favorable HER kinetics allow it to act as an expansion of the cathodic site where HER occurs, which increases the total rate of corrosion. Fig. 1d displays this, showing a striking amount of Zn dissolution after only 20 min in the electrolyte. Fig. S4 shows that the Cu surfaces of foils 2 and 4 were both largely covered in ZHS precipitates after 20 min of soaking, which would be expected if HER is significantly driven on those surfaces. The panels directly below in Fig. 1d display the relative lack of dissolution of Zn from Ti on foils 3 and 4 over the same time span compared to foil 2. Instead, the Zn plated on Ti on foil 3 delaminates significantly from the substrate. The plated Zn on foil 4 also shows significant delamination without much apparent dissolution of Zn. The relative lack of apparent dissolution from foil 4 compared to foil 2 could be due to the significantly smaller size of Cu foil exposed to the electrolyte in the former case.

Using these observations, we propose mechanisms for Zn corrosion both on Cu and Ti current collectors, as seen in Fig. 1e. When Zn is plated on Cu and exposed to a mildly acidic Zn electrolyte, the anodic oxidation and dissolution of Zn spontaneously occur on the plated Zn surface. Since both Zn and Cu can drive HER both surfaces can contribute to the cathodic half-reaction. Given that bubbling of H_2 gas is primarily observed on the Cu current collector rather than the plated Zn, it is likely that the Cu acts as the primary cathodic site. The result shown in the top half of Fig. 1e is a mostly split anodic and cathodic site where corrosion products like ZHS primarily form on Cu, and Zn dissolution occurs at the plated Zn surface. Importantly, this mechanism largely avoids the passivation of Zn from precipitated ZHS, thus promoting a rapid dissolution rate of plated Zn that scales in proportion to the size of the exposed Cu surface. In contrast, the Ti current collector largely suppresses HER on its surface as evidenced by the lack of bubble nucleation. This results in both the cathodic and anodic reactions becoming largely confined to the plated Zn surface, as seen in the bottom half of Fig. 1e. Consequently, ZHS will precipitate directly on the plated Zn, passivating it as it

corrodes. The resulting concentration of corrosion products and H_2 evolution on the plated Zn could lead to increased levels of dead Zn formation and delamination. The delamination may also be due to the relative lack of solubility between Zn and Ti *versus* Zn and Cu. Additionally, this could contribute significantly to the reported issue of H_2 bubble formation screening plated Zn from the electrolyte. This mechanism of corrosion of Ti would result in a slower but significant capacity loss profile and precipitation of ZHS directly on the plated surface of Zn.

To test these proposed mechanisms, we submerged Zn-plated Cu and Ti foils in 2 M $ZnSO_4$ for 6 h. Fig. S5 compares optical images of the two foils following this resting period and shows that the Zn appears to completely dissolve from the Cu surface, while it remains on the Ti surface with significant delamination. Fig. 1f shows SEM images and corresponding EDX maps of these two cases. Zn was originally plated in the top half of the images. As expected, the Zn signal is largely absent from where it was originally plated on the Cu foil, while the area surrounding the original plated area is covered in Zn from ZHS precipitation. In direct contrast, the Zn signal is largely confined to the original plated area on Ti, while the Ti surface remains mostly free of Zn and ZHS. In both cases, S and O signals were seen in the same regions as Zn, confirming that the Zn signal results from precipitation of corrosion products (Fig. S6).

The striking contrast between these two cases illustrates the importance of HER kinetics of a current collector in modeling and predicting corrosion in AZMBs. Depending upon whether the current collector takes on a significant amount of cathodic corrosion current, the corrosion mechanism can change significantly, resulting in different capacity loss profiles and distributions of corrosion products. Consequently, it is important to understand how cathodic corrosion is shared between Zn itself and the conducting substrates below it. While the foil soaking experiment provides a macroscopic view of this, the observation of bubble nucleation fails to provide an isolated, real-time view of the propagation of charge transfer across the current collectors. To track this spillover of charge onto the conductor, we turned to fluorescence microscopy imaging of the organic molecule resazurin (RZ) and its reduction to fluorescent resorufin (RF), as seen in Fig. 1g. By placing granular Zn particles on a transparent slide and dropping an aqueous solution containing RZ on top, we can visualize the spontaneous redox reaction between RZ and Zn^0 through the presence of fluorescence. Similarly to HER, the reduction of RZ to RF has thermodynamically favored compared to the oxidation of Zn as seen by the measured open circuit potential (Fig. S7). When performing this experiment on an insulating glass slide, the reduction of RZ, and hence the fluorescence, will be confined to the Zn surface like Zn corrosion on a Ti current collector (Fig. 1h). In contrast, when performed on a conductive indium tin oxide (ITO) coated glass slide, the reduction should spread across the entire surface, like Zn corrosion on a Cu current collector (Fig. 1h). By observing this spontaneous redox reaction on Zn in contact with either a conductor or an insulator with good time and spatial resolution, we can gain valuable insight into the propagation of the cathodic reaction in Zn corrosion on different current collectors.

"Unveiling" the cathodic site with fluorescence microscopy

We first dropped a solution of 1 mM RZ onto Zn particles on an insulating glass slide and, as expected, the reduction of RZ to RF was confined to the surface of Zn for the entirety of the experiment. Fig. 2ai–iii shows the progression of this reaction at 20 s, 40 s, and 60 s, respectively. In contrast, when Zn was placed on ITO, the reduction was shared between the Zn surface and the ITO slide, displaying a dynamic relationship between the two cathodic sites over time, as seen in Fig. 2bi–iii. Video S2 displays a side-by-side comparison of the two cases. We compared the fluorescent signal intensities both 10 μm and 500 μm from the Zn particles in each case in Fig. 2c to gain a more quantitative understanding of the distribution of the cathodic reaction. When the insulating glass slide is used, the fluorescence intensity reaches a relatively steady value after approximately 20 s, likely indicating a regime where the reduction of RZ to RF is limited by the mass transfer of RZ to the Zn surface. The intensity 500 μm away from Zn on glass increased only slightly as fluorescent RF diffused away from the Zn surface where it was produced. In contrast, when ITO is used, both intensity profiles shift significantly throughout the experiment time. Initially, the fluorescence intensity is highest near the surface of Zn, but this quickly levels off and even slightly decreases after 5 s. This decrease is met with a corresponding increase in intensity from the surrounding ITO surfaces far from Zn. Another interesting phenomenon is the appearance of rings of increased fluorescence around the Zn particles as seen in Fig. 2bi. These rings likely indicate a concentration profile that has formed around the Zn particles due to the initially high rate of RZ reduction on the Zn surface. This would introduce a mass transfer resistance, m_0, disfavoring reduction in this concentration depleted region.[46] Their formation occurs after several seconds and is followed by an increase in reduction rates far away on the ITO surface where the RZ concentration remains closer to the bulk concentration (see Video S2). After 20 s, the fluorescence intensities near the Zn surface and far away equal each other and appear from that time forward to increase at similar rates, indicating the presence of a competitive equilibrium between reduction on the Zn and ITO surfaces.

To further visualize the influence of RZ concentration on the distribution of cathodic current across the ITO surface, we repeated our initial experiment with the same amount of Zn, but with 50 μM RZ instead of the original 1 mM. This experiment should deplete the RZ around Zn quicker since the rate of reduction will be the same on Zn, but there is significantly less RZ present in solution. This will exaggerate the effects of concentration polarization on the system, creating a larger m_0. Indeed, we see an exaggerated effect of m_0 around the Zn particles with significant areas of low fluorescence surrounding them after 60 s, as seen in Fig. 2d and Video S3, compared with the ring of fluorescence in the more concentrated case. Fig. 2e displays the intensity across the blue line in the microscopy

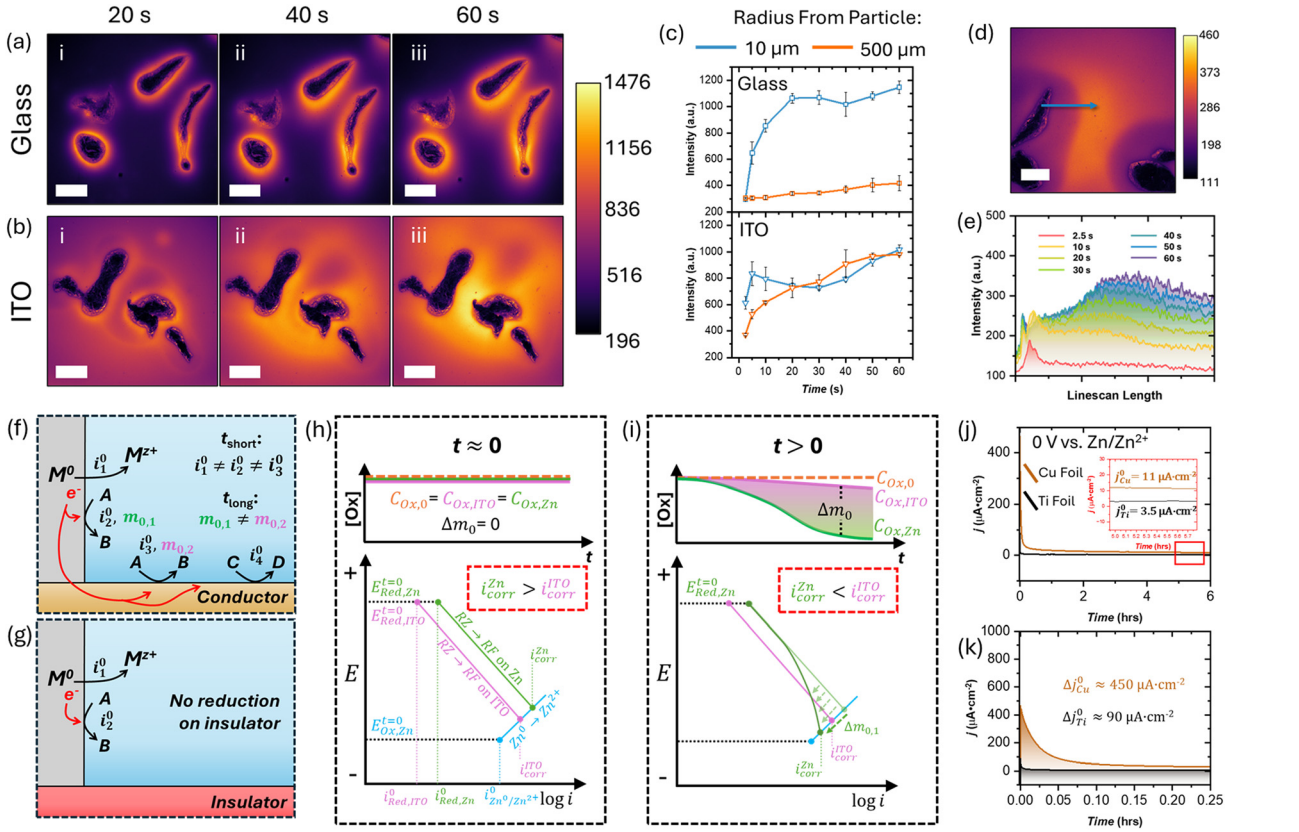

Fig. 2 (a) Fluorescence microscopy of 1 mM resazurin (RZ) reduction to resorufin (RF) on non-conducting glass (i) 20 s (ii) 40 s and (iii) 60 s after dropping the aqueous solution on the slide. (b) Fluorescence microscopy of 1 mM RZ reduction on conducting ITO coated glass (i) 20 s (ii) 40 s and (iii) 60 s after dropping the aqueous solution on the slide. (c) Intensity profiles over time of points 10 μm and 500 μm away from Zn particles on non-conducting glass (top) and conducting ITO coated glass (bottom). (d) Fluorescence microscopy of 50 μM RZ on ITO coated glass 60 s after dropping the aqueous solution on the slide. (e) Fluorescence intensity profiles over time along the blue line in (d). Scale bars are 500 μm for all fluorescence images. (f) Schematic depicting competing cathodic half reactions during spontaneous redox exchange with Zn on a conductor. (g) Schematic showing the simplified system when Zn is placed on an insulator. (h) Concentration profile and corresponding Evans diagram immediately after corrosion begins. (i) Concentration profiles and Evans diagram after oxidized species concentrations near the Zn and ITO surfaces deviate from the bulk concentration. (j) Current density *versus* time (*j*–*t*) curves for Cu and Ti working electrodes held at open circuit potential (OCP) *versus* a Zn foil in 2 M $ZnSO_4$ for 6 h. Inset shows the steady state *j* after 5 h for each foil. (k) Zoomed in *j*–*t* curve showing the decay in *j* for both foils over the first 15 min of the reaction.

image and shows the formation of this depletion zone within 20 s and its spread over time. While the intensity is initially highest at the Zn surface, it quickly depletes while the intensity far away on the ITO increases, significantly surpassing the intensity within the depleted zone. The depletion zone can also be seen expanding further away from the particles as time goes on. The observations confirm that m_0 has a major influence on the spread of cathodic current. In the cases using ITO as the substrate, the entire surface became significantly involved in the cathodic reaction in a matter of seconds and the overall amount of RZ reduction was significantly higher compared to those on glass. Since the only significant source of electrons in this system is the Zn particles themselves, this naturally leads to a faster dissolution rate. These observations provide insight into the extent that a large surface of exposed Cu increases the overall rate of Zn corrosion during resting. They also indicate what factors such as reaction kinetics and m_0 have a significant influence on the distribution of charge transfer. To demonstrate the applicability of this experiment to the acidic corrosion of Zn, we placed Zn powder on an ITO slide with a Pt wire in contact far away from the Zn (Fig. S8). The Pt was not attached to any external circuit. We pipetted 0.1 M HCl onto the ITO slide in contact with both the Zn and Pt wire. Immediately, the Zn began to corrode and the Pt wire far away began bubbling immediately due to its fast HER kinetics, demonstrating the charging of the ITO surface (Video S4). Meanwhile, there was no obvious bubbling on ITO due to its relatively slow HER kinetics compared to Pt.

Using mixed potential theory and the observations made through fluorescence microscopy, we can now create a model for the system that can be applied to the spontaneous corrosion of Zn while resting on different current collectors. Fig. 2f illustrates the reaction system taking place when a reactive metal, such as Zn, is placed on a conductor in the presence of oxidizing species such as RZ, H^+, H_2O, O_2, or any number of other molecules. The spontaneous reaction of Zn with these oxidants can each be separated into cathodic and anodic half-reactions that occur at the same rate to maintain electro-neutrality. While the anodic reaction in Zn corrosion is always

some form of Zn oxidation, the different cathodic reactions can occur on the Zn or on the conductor, with each reaction having unique exchange currents, i^0, and formal potentials, E^0. In contrast, when the Zn is placed on an insulator, the cathodic half reactions can only occur directly on the Zn surface, as seen in Fig. 2g. The value of i^0 for these cathodic reactions is determined by eqn (3), and depends on the heterogeneous rate constant, k^0, the electrode area, A, and the concentration of the oxidized reactant, C^*_{Ox}, where n is the number of electrons and F is Faraday's constant.

$$i^0_{Cat} = nFAk^0C^*_{Ox} \quad (3)$$

We can visualize the competing thermodynamic and kinetic factors and how they affect the overall corrosion current, i_{Corr}, using Evans diagrams. For the sake of simplicity, we will focus only on the reduction of RZ to RF and the oxidation of Zn. When the Zn and RZ initially meet, the concentrations of RZ at the surface of Zn, $C_{RZ,Zn}$, RZ at the ITO surface, $C_{RZ,ITO}$, and the bulk concentration of RZ, $C^*_{RZ,0}$, all equal each other, meaning that there will be no m_0 introduced to the different cathodic half reactions on each surface. The Evans diagram for $t \approx 0$ shows that the relative rates of RZ reduction on Zn and ITO depend on the exchange currents of reduction on either surface, $i^0_{Red,Zn}$ and $i^0_{Red,ITO}$, when there is no Δm_0 between the two. A higher $i^0_{Red,Zn}$ as shown in Fig. 2h will result in a higher initial rate of RZ reduction on Zn, i^{Zn}_{Corr}, as we observed. As the reaction proceeds long enough to deplete RZ around the Zn, a Δm_0, will occur between the Zn and ITO cathodic pathways. This will effectively curve the line for RZ reduction on Zn in a Tafel manner and decrease i^{Zn}_{corr} as illustrated in the corresponding Evans diagram in Fig. 2i. This will slow the rate of reduction on Zn and favor that on ITO, i^{ITO}_{Corr}, making $i^{Zn}_{Corr} > i^{ITO}_{Corr}$. Essentially, as the m_0 of one reaction pathway increases it lowers its respective i_{Corr}. Other areas with smaller m_0 values will have relatively higher i_{Corr} until they deplete the local C_{RZ} to a similar level. While i^{Zn}_{Corr} is limited to the small surface of Zn, i^{ITO}_{Corr} will spread its depletion of RZ over a much larger surface. This allows it to reduce less RZ at any given point on the ITO surface than on the Zn surface. The relative favoring of RZ reduction on ITO *versus* Zn will start reducing RZ on ITO close to the Zn due to the added resistance of ITO itself, R_{ITO}, which is not a perfect conductor, hence why the ring of increased fluorescence forms around the Zn particles in Fig. 2b and spreads further away over time. It marks the point at which both R_{ITO} and m_0 are minimized, resulting in the highest i_{Corr} at that point. Eventually, when $i^{Zn}_{Corr} \approx i^{ITO}_{Corr}$, the combined resistances of each pathway will self-regulate and maintain the currents at similar values. On glass, this competitive equilibrium will not exist. Rather, i^{Zn}_{Corr} will likely decrease until a steady state with RZ diffusion to the Zn surface is achieved, at which point m_0 will no longer increase.

This model can now be applied to explain the phenomena observed in Zn corrosion during resting by substituting RZ reduction with HER. Our observations, along with literature, suggest that Cu has a much higher HER exchange current, $i^0_{HER,Cu}$, than that of Ti, $i^0_{HER,Ti}$.[47–49] This difference comes from the intrinsic k^0 values of each material for HER and is also reflected in the HER overpotentials on each material in Fig. S1. It is also important to note that increasing the exposed area of the current collector will also significantly increase i^0. To visualize current collector dependent corrosion rates, we used either a Cu or Ti foil as a working electrode and a Zn foil as the reference/counter electrode submerged in 2 M $ZnSO_4$ and applied 0 V. This technique holds the system at open circuit potential (OCP) without limiting the current passed, which electrochemically mimics the resting state. The resulting current density, j, is the corrosion current density, j_{Corr}, on Cu or Ti. Fig. 2j shows the j–t curves over the course of 6 h. After several hours, j^{Cu}_{Corr} and j^{Ti}_{Corr} have relatively similar values of 11 μA cm^{-2} and 3.5 μA cm^{-2}. While these j_{Corr} values are similar to others reported in the same electrolyte, the difference is much smaller than literature i^0 values would suggest[41]. Additionally, it is doubtful that such a small difference in j_{Corr} would result in the differences in distribution of bubbling and ZHS formation seen in Fig. 1. Upon further inspection though, the j–t curves differ significantly in the first several minutes of corrosion (Fig. 2k). While j^{Ti}_{Corr} decays from an initial maximum to a steady state value within seconds, it takes j^{Cu}_{Corr} several minutes to decay to a nearly steady state, where it continues to decay slightly throughout the entire experiment. While the decay on Ti is likely from the inherent capacitive current after applying an electrode bias, the time scale of decay on Cu suggests that a faradaic process occurring. This $\Delta j^{Cu}_{Corr} \approx$ 450 μA cm^{-2} and likely corresponds to the rapid passivation of the Cu surface as it corrodes in contact with Zn in the acidic electrolyte. The time scale of several minutes for this Δj^{Cu}_{Corr} is reasonable when considering the observations that the entire ITO surface aided in RZ reduction almost instantaneously, and that bubbles were observed across the entire Zn-plated Cu foil within 1 minute of electrolyte exposure. These observations now provide a clearer view of how the current collector affects resting Zn corrosion. We see that several factors govern the i_{corr} such as solution m_0, and both the k^0 and A of the current collector. Additionally, the current collector influence can change as corrosion occurs if it is passivated by the reaction, as we see with Cu. With this in mind, we turned to *in situ operando* ECMS to provide a quantitative view of how different current collector materials affect i_{corr}.

Quantifying substrate dependent corrosion rates with ECMS

ECMS allows us to track the evolution of gases, such as H_2, while performing an electrochemical reaction. Fig. 3a shows the experimental setup with a working electrode and a Zn reference/counter electrode in 2 M $ZnSO_4$. As we applied 0 V for 10 minutes, all evolved gases were captured *via* the membrane chip and carried to a quadrupole mass analyzer by an Ar carrier gas. Several working electrodes were used including Cu, Ti, Zn, SS, glassy carbon (C), and a Pt-plated C electrode (referred to as Pt). Fig. S9 shows the electrode and electrochemical cell setup used for the ECMS experiments. A calibration process was used to convert mass analyzer signals for H_2 into

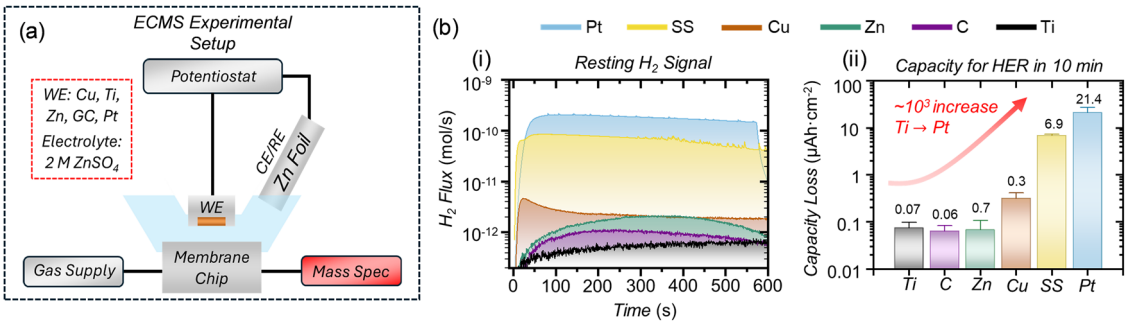

Fig. 3 (a) Schematic of electrochemical mass spectrometry (ECMS) experimental setup. Working electrode (WE) materials are marked in the legend and Zn foil was used as a counter/reference electrode (CE/RE). (b) (i) H_2 flux to the mass spectrometer over time when 0 V was applied *vs.* Zn^0/Zn^{2+} in 2 M $ZnSO_4$ for different WE materials and (ii) capacity lost for each WE material after resting at OCP for 10 min.

molar values of H_2 flux (Fig. S10). Fig. S11 shows the raw H_2 mass analyzer signals before baseline correction and calibration. Fig. 3bi shows the H_2 flux profiles of each electrode while resting at OCP for 10 minutes and Fig. 3bii shows the integrated capacity loss due to HER in each case. Ti produced the least amount of H_2 with C and Zn producing slightly more. The flux profile for Cu shows an initial spike in H_2 flux followed by a slightly higher steady state than Ti, C and Zn, which agrees well with the observations of j_{Corr}^{Cu} in Fig. 2k. There was a significant increase in H_2 flux when using a SS electrode, which was not surprising given its favorable HER kinetics. The H_2 flux increased further when using the Pt electrode, despite not having complete coverage of the C electrode (Fig. S12).

These observations highlight several important points regarding resting corrosion rates on AZMB anodes. First, while spontaneous HER on Zn itself is the root cause of corrosion, the intrinsic rate of this reaction is relatively low compared to some of the other materials used. For example, Cu produces a higher H_2 flux even after passivation, which explains why H_2 bubbles were primarily observed on Cu rather than Zn in Fig. 1. Next, the material on which Zn is plated while resting can change the rate of corrosion by nearly three orders of magnitude. Consequently, researchers should treat all conductive surfaces that are electrically and electrolytically connected to corroding Zn as participants in the reaction and account for the i_{Corr} of each material. While a Ti or C current collector might not increase the rate of corrosion significantly, an SS or Pt electrode will immediately multiply the rate by several orders of magnitude. Therefore, failure to account for the current collector and other connected surfaces could lead to misinterpretations of corrosion rates and mechanisms in different systems.

Yet another important point is that a passive current collector does not necessarily mitigate all resting corrosion issues. In fact, our trend for HER rates on each current collector material given by ECMS does not perfectly match the trend of % CE lost while resting. While Zn plated on Pt and SS experience the worst and fastest losses, Ti has been reported to experiences larger % CE losses than Cu, as discussed in Fig. 1. This is due to the other mechanisms in addition to Zn dissolution such as bubble nucleation and delamination. Therefore, it is important to not only choose a passive current collector, but also to take measures to mitigate the other Zn loss mechanisms that will be promoted by that passivity. One possible solution is presented by high current density plating during cycling, which has been shown to promote a uniform coverage of relatively small Zn nuclei and the formation of a uniform SEI layer.[21] Not only would this SEI passivate a current collector like Cu, but the small Zn nuclei might also discourage delamination and nucleation of large, screening H_2 bubbles.

Many AZMB systems opt to use a Zn foil as an anode material instead of a separate current collector material (Cu, Ti, SS, C, *etc.*). This will also affect the rate and mechanism of spontaneous resting corrosion at the anode. We see in Fig. 3b that the inherent rate of HER on Zn surfaces is relatively similar to the rates on C and Ti, so the overall chemical rate of corrosion may be similar to a case using those current collector materials. However, using a Zn current collector will likely result in less delamination given that the adhesion between plated Zn and a Zn foil will be better than that between plated Zn and Ti or C. However, the other issues that remain when the corrosion mechanism is primarily focused on the anode active material (Zn) such as screening bubble formation, precipitation of non-uniform SEI layers and dead Zn formation will likely remain persistent.

Another important consideration is the changing ratio of exposed current collector *versus* plated Zn at different charging current densities. For example, plating Zn on a current collector at 10 mA cm^{-2} will result in more uniform nucleation and higher surface coverage than plating at 1 mA cm^{-2}. We visualize this on a Cu foil to show that plating Zn at 1 mA cm^{-2} for 1 mAh cm^{-2}, as used in the % CE tests in Fig. 1, results in a much larger area of current collector in contact with the electrolyte than plated Zn (Fig. S13). At 5 mA cm^{-2} and 10 mA cm^{-2} for the same areal capacity the area of exposed current collector was closer to equal to that of Zn in both cases (Fig. S13). Additionally, we plated Zn on Cu foils and examined the evolution of both the morphology and microstructure of both the plated Zn and an area of the Cu foil far from the Zn (Fig. S14). We found that the Zn visibly dissolved while resting in 2 M $ZnSO_4$ after 24 h and 48 h. In SEM, the morphology changed while resting from islands of plated Zn to large flakey structures indicative of ZHS formation. XRD also confirmed the

disappearance of Zn signal and formation of ZHS. As expected, ZHS was formed both at the cites where Zn was plated and far away on the Cu. Overall, these data demonstrate that there will be current collector exposed to partake in corrosion even at high practical current densities. In cases where there is little to no current collector exposed (either due to extreme charging current densities or using Zn foil as a current collector) the corrosion mechanism will be focused on the Zn itself, leading to an emphasis on Zn passivation, dead Zn formation and screening bubble formation as opposed to dissolution.

In addition to considering how the charging current density might affect the corrosion rate and mechanism in light of the current collector involvement, we must also consider the impact of areal capacity. In general, a higher areal capacity of plated Zn will result in less exposed current collector surface. In cases where an active current collector material such as Cu is used, a higher areal capacity of plated Zn will reduce the exposed surface area of Cu that is responsible for increasing the corrosion rate and favoring dissolution of Zn. Indeed, it is reported in literature that % CE loss during resting periods decreases with increased areal capacity when plating Zn on a Cu foil (Fig. S15).[39]

We must consider slightly different factors when Zn is plated on Ti. While Ti does not have high HER activity, and will not catalyze Zn dissolution, it is apparent that the interface of plated Zn and Ti is a preferred point of delamination. Therefore, it may also be favorable to have a high coverage of Zn with little exposed current collector in this case. Literature has shown that Ti also has lower % CE losses at higher areal capacities, albeit with a less consistent trend than Cu (Fig. S15).[40] In the case of using a Zn foil current collector, we would expect a less apparent trend of % CE loss with varying area capacity for the reasons discussed when considering the impact of current density. While the current work demonstrates the key role of the current collector material in resting corrosion, there remains a certain level of uncertainty about the intricacies of each of the proposed corrosion mechanisms (Zn dissolution, dead Zn formation, delamination, H_2 bubble screening, *etc.*). Therefore, the direct real-time observation of these different corrosion mechanisms at the micro scale remains a highly interesting avenue of inquiry that could have a significantly positive impact on the field of AZMBs and beyond.

Finally, when considering how these corrosion mechanisms translate from bulk corrosion and ECMS experiments to a coin or pouch cell during battery cycling, we must consider both chemical and mechanical differences. Given that corrosion is governed by the thermodynamically favorable chemical reaction between plated Zn^0 and H^+ in solution, it is not likely that the rate will be altered significantly by the differences in pressure or the concentration of dissolved gas that might be present in batteries *versus* the bulk environment. Rather, the reaction is primarily influenced by chemical factors such as HER kinetics on various substrates present and the pH of solution, both of which will remain relatively consistent between bulk or ECMS experiments and coin or pouch cells. Therefore, the main differences will be mechanical resulting from gas formation. In bulk experiments, and especially in ECMS, evolved gas will tend to not stay on the corroding surfaces. However, in coin and pouch cells, several works have shown that these bubbles will stay and lead to battery swelling and screening of the anode from solution.[40,41] It is also worth noting that the screening effect from H_2 bubble formation will primarily affect areas that have already been significantly corroded and therefore somewhat passivated. Consequently, while the trapping of produced gases in a closed battery system during resting may not cause significant changes in corrosion rate chemically, it will likely lead to significant problems for battery stability and safety due to mechanical stresses on the battery cells.

Implications beyond resting capacity loss

This newfound understanding of the influence of current collectors on reactions in AZMBs can also shed light on other phenomena that are not well understood. Most coin cell failures are indicated either by an abrupt drop of the polarization voltage to 0 V, or a sharp increase to voltages far above typical values expected for nucleation and growth of Zn on the anode. Literature ascribes these to short circuiting and corrosion products forming on the surface of the anode.[50–52] While it makes sense that the voltage would drop to 0 in the case of a short circuit, the explanation of the abrupt increases being based purely on SEI products forming on the anode surface is less clear. Many works demonstrate the formation of a uniform SEI improves the cycling of coin cells while inducing marginal and stable increases in polarization voltage.[53–55] Essentially, the precipitation of a stable SEI results in a slight increase in resistance. However, the large abrupt spikes in polarization voltage seen in failing coin cells would require massive increases in resistance given the linear relationship between E and R in Ohm's Law. Despite this, many works offer the formation of corrosion products as an explanation for why their coin cells began jumping to high polarization voltages and failed shortly thereafter. The spikes in voltage are most often attributed to the formation of a non-uniform SEI layer, which could lead to several failures in battery integrity such as short circuits and dead Zn. Despite this, there is little consensus or direct evidence on the exact mechanisms of these failures. Therefore, it is of high interest to the scientific community to investigate and elucidate the intricacies of these failure mechanisms.

One possible explanation presents itself when considering that the entire system can share in the corrosion when exposed to electrolyte and electrically connected to Zn. Applying this to a scenario where a coin cell was overfilled with excess electrolyte, causing the solution to contact the SS case, it is now apparent that the SS case might present a significant problem. The case would immediately partake in the corrosion reaction, both increasing its overall rate and precipitating corrosion products on the surface of SS. Fig. 4a depicts a proposed mechanism of how the precipitation of ZHS on SS in this manner could compromise the electrical conductivity of the coin cell by forming precipitates between the case and current collector.

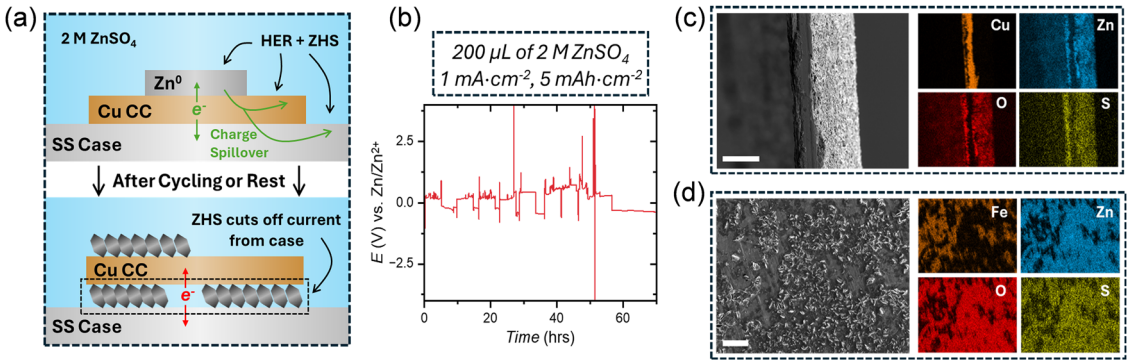

Fig. 4 (a) Schematic depicting the buildup of ZHS corrosion on both the Cu current collector (CC) and stainless steel (SS) case of a Zn coin cell while resting, and the resulting shutoff of current. (b) Voltage *versus* time (*E*–*t*) profile for a Cu|Zn asymmetric cell with 200 µL of 2 M $ZnSO_4$ electrolyte cycled at 1 mA cm^{-2} with a capacity of 5 mAh cm^{-2}. (c) SEM and corresponding EDX images of a Zn-plated Cu CC and that was placed on a SS case and submerged in 2 M $ZnSO_4$ for 1 h. (d) SEM and corresponding EDX images of the submerged SS case after removal of the electrolyte and Cu CC.

Given that ZHS is ionically conducting, but electrically insulting, its presence on the top of the current collector would still allow for Zn plating and might not cause the battery to fail. However, its presence between the current collector and the SS case would cause current to be cut off from the current collector, introducing a spike in *R* and therefore a spike in *E*. To test this, we overfilled a coin cell separator for a Cu|Zn coin cell with 200 µL of 2 M $ZnSO_4$ and cycled it with a capacity of 5 mAh cm^{-2} at 1 mA cm^{-2}. The resulting *E*–*t* curve in Fig. 4b shows the presence of abrupt spikes in polarization voltage as we would expect. We tested this mechanism further by plating Zn on a Cu current collector and then placing the foil onto an open SS coin cell case. We then pipetted in 2 M $ZnSO_4$ and waited 1 h. Fig. 4c shows a cross-sectional view of the Cu current collector with ZHS on both sides and Fig. 4d shows the SS case with ZHS across the surface – indicating significant precipitation in between the two. This shows that through the rapid spread of corrosion, SS coin cell components will corrode if electrically and electrolytically connected to Zn, despite no potential being applied and no Zn plated on the SS. This in turn, can lead to sudden and catastrophic failure of coin cells. We further tested the prevalence of this corrosion mechanism at smaller electrolyte volumes (Fig. S16). At electrolyte volumes as low as 100 µL there is significant corrosion across the surface of the SS components including the areas covered by the current collectors. At lower volumes, the corrosion is limited to areas of SS outside the perimeter of the current collector, rather than in between the SS and current collector. Given these observations, the presence of corrosion on SS components in coin cells could be a major contributor to coin cell failure at high electrolyte volumes ($\geq$100 µL) and will likely accelerate resting losses *via* favorable HER kinetics even at low electrolyte volumes. While it is not the sole cause of voltage spikes in coin cell cycling, it represents an often-ignored contributing factor that can be mitigated by either using small electrolyte volumes or inert coin cell components.

In addition to HER occurring during resting periods in AZMB's it has been widely reported that HER will also occur while plating Zn.[17] This is most often attributed to the simultaneous reduction of H_2O when applying a cathodic current to reduce solvated Zn^{2+}. However, less attention has been given to HER during stripping of Zn, with only one recent work reporting HER due to galvanic corrosion of Zn in this regime.[56] Given the observations of this work, the mixed potential theory framework applied to Zn resting corrosion throughout this work suggests that corrosion may be possible in a similar manner while stripping without the cathodic protection provided to Zn during plating. We tested this using a Zn WE and a Zn foil CE/RE in 2 M $ZnSO_4$. Importantly, the CE/RE was removed from the ECMS cell and connected with a salt bridge to avoid detecting HER from the CE while stripping from the Zn WE (Fig. S17). Fig. S18 displays the H_2 signal before baseline correction and calibration. Surprisingly, we not only observed H_2 evolution during Zn stripping, but determined that the H_2 flux during galvanostatic stripping was comparable to that of plating (Fig. 5a). This observation is especially intriguing given that significant amounts of cathodic HER occur on the working electrode while an anodic current is galvanostatically driven at a highly positive polarization voltage. In this state, no cathodic reactions are being driven by the potentiostat at the working electrode. This suggests that galvanic exchange is occurring between plated Zn and H^+ outside of the controlled circuit of the potentiostat. We again tested this system without separating the counter electrode *via* salt bridge and found that while the polarization voltage was much smaller than in Fig. 5a, the significant H_2 flux during stripping remained (Fig. S19). We further tested this mechanism by doing cyclic voltammetry of both Zn stripping and plating in a 10 mM $ZnSO_4$ solution with a Zn WE, a 1 M Ag/AgCl RE and Pt CE. Fig. 5b shows the H_2 flux plotted over the *E*–*t* and *i*–*t* curves for the cyclic voltammogram showing that the evolution of H_2 is strikingly consistent both for stripping and plating of Zn. The uncorrected H_2 signal is shown in Fig. S20. These results reveal that H_2 evolves throughout the Zn cycling process during both plating and stripping, suggesting that galvanic corrosion of Zn plated on various current collectors is not merely limited to resting periods. Importantly, this implicates the materials used as current collectors as potentially having a significant influence on corrosion during active battery cycling in addition to resting.

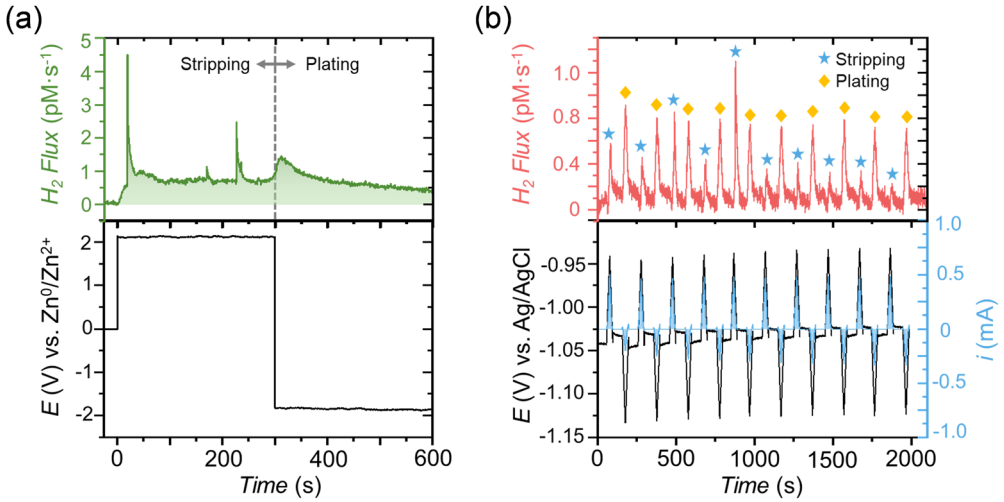

Fig. 5 (a) H_2 flux profile and E–t profile for galvanostatic stripping and plating of Zn at 1 mA cm^{-2} in 2 M $ZnSO_4$ on a Zn WE. (b) H_2 flux profile and both E–t and i–t profiles for cyclic voltammetric stripping and plating of Zn in 10 mM $ZnSO_4$ on a Zn WE. The potential window was ±100 mV from the OCP.

Our group is now working to further investigate the mechanism of galvanic corrosion during cycling in addition to resting periods.

Conclusion

This work establishes the mechanistic origins of high resting losses in AZMBs, both providing a comprehensive explanation for why capacity fading is dramatically higher than in analogous non-aqueous Li and Na systems and highlighting corrosion pathways unique to Zn. Using fluorescence microscopy, we visualize the time and spatially resolved lateral propagation of cathodic current across current collectors, showing that spontaneous electron exchange occurs not only on deposited Zn but also on the current collector itself, significantly affecting corrosion rates and mechanisms across the system. These observations provide rare, direct insight into heterogeneous electron transfer spreading from a single source across conductive surfaces – offering visual evidence of mixed potential theory and illustrating the striking speed at which charge propagates through conductors in contact with the source of spontaneous electron exchange. Employing *in situ operando* ECMS, we precisely quantify resting corrosion rates and faradaic efficiencies, demonstrating that these rates can vary by several orders of magnitude depending on the HER kinetics of the current collector, establishing the critical role of material selection in controlling corrosion. Mechanistically, our results show that galvanic corrosion extends beyond the anode to involve current collectors and other coin cell components such as casings, spacers, and springs whose catalytic activity toward HER exacerbates the corrosion process when in contact with the electrolyte – accelerating the rate of Zn loss and potentially electrically compromising the coin cell. Importantly, these hidden corrosion pathways also manifest during cycling, providing an explanation for surprising HER observations during Zn stripping. By systematically linking deposited Zn, current collectors, and non-electrode components, this study unifies prior observations of resting corrosion, provides a detailed mechanistic framework for capacity fading, and establishes rational design principles to mitigate losses. Collectively, these findings not only advance fundamental understanding of corrosion in AZMBs but also offer generalizable insights for other metal-anode systems, informing strategies to control spontaneous redox reactions and enhance long-term battery performance.

Author contributions

J. F. K., A. R., and M. A. F. performed conceptualization, investigation, methodology development and writing. J. H. N., S. P. and J. H. L. aided in investigation and methodology and reviewing. J. E. D. provided funding, supervision and conceptualization, and aided in writing. All authors reviewed and approved the final draft of the article.

Conflicts of interest

The authors have no conflicts of interest to declare.

Data availability

Raw data has been made available in the supplementary information (SI). Supplementary information is available. See DOI: **https://doi.org/10.1039/d5ee05063d**.

Further raw data files can be made available from authors upon reasonable request.

Acknowledgements

The authors were sponsored by the Army Research Office and Army Research Laboratory (ARL) under Grant # W911NF-24-1-0199. The views and conclusions contained in this document

are those of the authors and should not be interpreted as representing the official policies, either expressed or implied, of the Army Research Office, ARL, or the U.S. Government. The U.S. Government is authorized to reproduce and distribute reprints for Government purposes notwithstanding any copyright notation herein. The authors acknowledge the use of Chat-GPT 3.5 for language refinement. The authors would also like to acknowledge the use of facilities within the Purdue Electron Microscopy Center – Facility RRID SCR_022687.

References

1 C. Li, S. Jin, L. A. Archer and L. F. Nazar, Toward practical aqueous zinc-ion batteries for electrochemical energy storage, *Joule*, 2022, **6**(8), 1733–1738.
2 D. Kundu, B. D. Adams, V. Duffort, S. H. Vajargah and L. F. Nazar, A high-capacity and long-life aqueous rechargeable zinc battery using a metal oxide intercalation cathode, *Nat. Energy*, 2016, **1**(10), 1–8.
3 J. F. Parker, C. N. Chervin, I. R. Pala, M. Machler, M. F. Burz, J. W. Long and D. R. Rolison, Rechargeable nickel–3D zinc batteries: An energy-dense, safer alternative to lithium-ion, *Science*, 2017, **356**(6336), 415–418.
4 X. Shi, J. Xie, F. Yang, F. Wang, D. Zheng, X. Cao, Y. Yu, Q. Liu and X. Lu, Compacting electric double layer enables carbon electrode with ultrahigh Zn ion storage capability, *Angew. Chem., Int. Ed.*, 2022, **61**(51), e202214773.
5 Z. Zhu, T. Jiang, M. Ali, Y. Meng, Y. Jin, Y. Cui and W. Chen, Rechargeable batteries for grid scale energy storage, *Chem. Rev.*, 2022, **122**(22), 16610–16751.
6 B. Tang, L. Shan, S. Liang and J. Zhou, Issues and opportunities facing aqueous zinc-ion batteries, *Energy Environ. Sci.*, 2019, **12**(11), 3288–3304.
7 L. Cao, D. Li, E. Hu, J. Xu, T. Deng, L. Ma, Y. Wang, X.-Q. Yang and C. Wang, Solvation structure design for aqueous Zn metal batteries, *J. Am. Chem. Soc.*, 2020, **142**(51), 21404–21409.
8 Y. Zhu, Y. Cui and H. N. Alshareef, An anode-free Zn–MnO_2 battery, *Nano Lett.*, 2021, **21**(3), 1446–1453.
9 F. Wang, O. Borodin, T. Gao, X. Fan, W. Sun, F. Han, A. Faraone, J. A. Dura, K. Xu and C. Wang, Highly reversible zinc metal anode for aqueous batteries, *Nat. Mater.*, 2018, **17**(6), 543–549.
10 I. Aguilar, J. Brown, L. Godeffroy, F. Dorchies, V. Balland, F. Kanoufi and J.-M. Tarascon, A key advance toward practical aqueous Zn/MnO2 batteries via better electrolyte design, *Joule*, 2025, **9**(1), 101784, DOI: 10.1016/j.joule.2024.11.001.
11 J.-Y. Luo, W.-J. Cui, P. He and Y.-Y. Xia, Raising the cycling stability of aqueous lithium-ion batteries by eliminating oxygen in the electrolyte, *Nat. Chem.*, 2010, **2**(9), 760–765.
12 L. Ma, Q. Li, Y. Ying, F. Ma, S. Chen, Y. Li, H. Huang and C. Zhi, Toward Practical High-Areal-Capacity Aqueous Zinc-Metal Batteries: Quantifying Hydrogen Evolution and a Solid-Ion Conductor for Stable Zinc Anodes, *Adv. Mater.*, 2021, **33**(12), 2007406, DOI: 10.1002/adma.202007406.
13 X. Yu, Z. Li, X. Wu, H. Zhang, Q. Zhao, H. Liang, H. Wang, D. Chao, F. Wang and Y. Qiao, Ten concerns of Zn metal anode for rechargeable aqueous zinc batteries, *Joule*, 2023, **7**(6), 1145–1175.
14 J. Cao, D. Zhang, X. Zhang, Z. Zeng, J. Qin and Y. Huang, Strategies of regulating Zn_{2+} solvation structures for dendrite-free and side reaction-suppressed zinc-ion batteries, *Energy Environ. Sci.*, 2022, **15**(2), 499–528, DOI: 10.1039/D1EE03377H.
15 T. Wang, C. Li, X. Xie, B. Lu, Z. He, S. Liang and J. Zhou, Anode Materials for Aqueous Zinc Ion Batteries: Mechanisms, Properties, and Perspectives, *ACS Nano*, 2020, **14**(12), 16321–16347, DOI: 10.1021/acsnano.0c07041.
16 A. Rana, K. Roy, J. N. Heil, J. H. Nguyen, C. Renault, B. M. Tackett and J. E. Dick, Realizing the Kinetic Origin of Hydrogen Evolution for Aqueous Zinc Metal Batteries, *Adv. Energy Mater.*, 2024, **14**(43), 2402521.
17 A. Rana, M. A. Faisal, J. H. Nguyen, S. Paul, J. F. Koons, J. H. Lawrence, K. Roy and J. E. Dick, An Electroanalytical Perspective on the Competitive Interplay between Zinc Deposition and Hydrogen Evolution in Aqueous Zinc Metal Batteries, *Adv. Energy Mater.*, 2025, e03630, DOI: 10.1002/aenm.202503630.
18 Y. Yang, H. Yang, R. Zhu and H. Zhou, High reversibility at high current density: the zinc electrodeposition principle behind the ''trick'', *Energy Environ. Sci.*, 2023, **16**(7), 2723–2731.
19 H. Yang, Y. Yang, W. Yang, G. Wu and R. Zhu, Correlating hydrogen evolution and zinc deposition/dissolution kinetics to the cyclability of metallic zinc electrodes, *Energy Environ. Sci.*, 2024, **17**(5), 1975–1983.
20 W. Yuan, X. Nie, G. Ma, M. Liu, Y. Wang, S. Shen and N. Zhang, Realizing Textured Zinc Metal Anodes through Regulating Electrodeposition Current for Aqueous Zinc Batteries, *Angew. Chem., Int. Ed.*, 2023, **62**(10), e202218386, DOI: 10.1002/anie.202218386.
21 A. Rana, S. Paul, A. Bhadouria, J. H. Nguyen, J. F. Koons, C. Li, A. Das, K. Roy, B. M. Tackett and J. E. Dick, Interfacial pH gradients suppress HER at high currents in zinc metal batteries, *Joule*, 2025, **9**, 102167, DOI: 10.1016/j.joule.2025.102167.
22 S. Paul, J. H. Nguyen, M. L. Harrigan, A. Rana, A. Berbille and J. E. Dick, Small changes, big gains: standardizing non-electrode coin cell components in aqueous zinc battery research, *EES Batteries*, 2025, **1**, 813–823, DOI: 10.1039/D5EB00084J.
23 G. Wu, Y. Yang, R. Zhu, W. Yang, H. Yang and H. Zhou, The pitfalls of using stainless steel (SS) coin cells in aqueous zinc battery research, *Energy Environ. Sci.*, 2023, **16**(10), 4320–4325.
24 Q. Li, A. Chen, D. Wang, Z. Pei and C. Zhi, ''Soft shorts'' hidden in zinc metal anode research, *Joule*, 2022, **6**(2), 273–279.
25 M. Kim, L. Pompizii, J. Byun, A. Coskun and J. W. Choi, The challenge of corrosion in next-generation rechargeable metal batteries, *Chem*, 2025, **11**(8), 102661, DOI: 10.1016/j.chempr.2025.102661.

26 B. Zhang and H. J. Fan, Overlooked calendar issues of aqueous zinc metal batteries, *Joule*, 2025, **9**(1), 101802, DOI: 10.1016/j.joule.2024.12.003.
27 Z. Wu, Q. Li, Z. Chen and C. Zhi, Calendar aging of zinc-ion batteries, *Matter*, 2025, **8**(5), 102137, DOI: 10.1016/j.matt.2025.102137.
28 L. Wang, Z. Zhao, Y. Yao, Y. Zhang, Y. Meng, B. Hu, J. Kang, J. Guo, L. Zhang and H. Lu, Highly fluorinated non-aqueous solid-liquid hybrid interface realizes water impermeability for anti-calendar aging zinc metal batteries, *Energy Storage Mater.*, 2023, **62**, 102920.
29 Z. Yang, Y. Sun, J. Li, G. He and G. Chai, Noncovalent Interactions-Driven Self-Assembly of Polyanionic Additive for Long Anti-Calendar Aging and High-Rate Zinc Metal Batteries, *Adv. Sci.*, 2024, **11**(33), 2404513.
30 P. Keil, S. F. Schuster, J. Wilhelm, J. Travi, A. Hauser, R. C. Karl and A. Jossen, Calendar aging of lithium-ion batteries, *J. Electrochem. Soc.*, 2016, **163**(9), A1872.
31 M. Naumann, M. Schimpe, P. Keil, H. C. Hesse and A. Jossen, Analysis and modeling of calendar aging of a commercial LiFePO4/graphite cell, *J. Energy Storage*, 2018, **17**, 153–169, DOI: 10.1016/j.est.2018.01.019.
32 D. T. Boyle, W. Huang, H. Wang, Y. Li, H. Chen, Z. Yu, W. Zhang, Z. Bao and Y. Cui, Corrosion of lithium metal anodes during calendar ageing and its microscopic origins, *Nat. Energy*, 2021, **6**(5), 487–494, DOI: 10.1038/s41560-021-00787-9.
33 D. Lin, Y. Liu, Y. Li, Y. Li, A. Pei, J. Xie, W. Huang and Y. Cui, Fast galvanic lithium corrosion involving a Kirkendall-type mechanism, *Nat. Chem.*, 2019, **11**(4), 382–389.
34 S. M. Wood, C. Fang, E. J. Dufek, S. C. Nagpure, S. V. Sazhin, B. Liaw and Y. S. Meng, Predicting calendar aging in lithium metal secondary batteries: the impacts of solid electrolyte interphase composition and stability, *Adv. Energy Mater.*, 2018, **8**(26), 1801427.
35 L. Streck, T. Roth, H. Bosch, C. Kirst, M. Rehm, P. Keil and A. Jossen, Self-discharge and calendar aging behavior of Li-ion and Na-ion cells, *J. Electrochem. Soc.*, 2024, **171**(8), 080531.
36 W. Kao-ian, R. Pornprasertsuk, P. Thamyongkit, T. Maiyalagan and S. Kheawhom, Rechargeable zinc-ion battery based on choline chloride-urea deep eutectic solvent, *J. Electrochem. Soc.*, 2019, **166**(6), A1063–A1069.
37 A. Konarov, N. Voronina, J. H. Jo, Z. Bakenov, Y.-K. Sun and S.-T. Myung, Present and future perspective on electrode materials for rechargeable zinc-ion batteries, *ACS Energy Lett.*, 2018, **3**(10), 2620–2640.
38 S. Thomas, N. Birbilis, M. S. Venkatraman and I. S. Cole, Corrosion of Zinc as a Function of pH, *Corrosion*, 2012, **68**(1), 015001–015009, DOI: 10.5006/1.3676630.
39 B. Liu, X. Yuan and Y. Li, Colossal capacity loss during calendar aging of Zn battery chemistries, *ACS Energy Lett.*, 2023, **8**(9), 3820–3828.
40 S. D. Pu, B. Hu, Z. Li, Y. Yuan, C. Gong, Z. Ning, C. Chau, S. Yang, S. Zhang and L. Pi, *et al.*, Decoupling, quantifying, and restoring aging-induced Zn-anode losses in rechargeable aqueous zinc batteries, *Joule*, 2023, **7**(2), 366–379, DOI: 10.1016/j.joule.2023.01.010.
41 Q. Li, Y. Wang, F. Mo, D. Wang, G. Liang, Y. Zhao, Q. Yang, Z. Huang and C. Zhi, Calendar life of Zn batteries based on Zn anode with Zn powder/current collector structure, *Adv. Energy Mater.*, 2021, **11**(14), 2003931.
42 Y. Yuan, Z. Li, R. Deng, S. D. Pu, M. Walker, M. Cai, F. Wu, P. G. Bruce and A. W. Robertson, Identifying the role of Zn self-dissolution in the anode corrosion process in Zn-ion batteries, *Energy Environ. Sci.*, 2025, **18**(11), 5610–5621, DOI: 10.1039/D5EE00485C.
43 J. Hao, B. Li, X. Li, X. Zeng, S. Zhang, F. Yang, S. Liu, D. Li, C. Wu and Z. Guo, An In-Depth Study of Zn Metal Surface Chemistry for Advanced Aqueous Zn-Ion Batteries, *Adv. Mater.*, 2020, **32**(34), 2003021, DOI: 10.1002/adma.202003021.
44 J. Hao, X. Li, S. Zhang, F. Yang, X. Zeng, S. Zhang, G. Bo, C. Wang and Z. Guo, Designing Dendrite-Free Zinc Anodes for Advanced Aqueous Zinc Batteries, *Adv. Funct. Mater.*, 2020, **30**(30), 2001263, DOI: 10.1002/adfm.202001263.
45 D. Li, L. Cao, T. Deng, S. Liu and C. Wang, Design of a Solid Electrolyte Interphase for Aqueous Zn Batteries, *Angew. Chem., Int. Ed.*, 2021, **60**(23), 13035–13041, DOI: 10.1002/anie.202103390.
46 A. J. Bard, L. R. Faulkner and H. S. White, *Electrochemical methods: fundamentals and applications*, John Wiley & Sons, 2022.
47 N. Pentland, J. M. Bockris and E. Sheldon, Hydrogen evolution reaction on copper, gold, molybdenum, palladium, rhodium, and iron: mechanism and measurement technique under high purity conditions, *J. Electrochem. Soc.*, 1957, **104**(3), 182.
48 N. T. Thomas and K. Nobe, Kinetics of the Hydrogen Evolution Reaction on Titanium, *J. Electrochem. Soc.*, 1970, **117**(5), 622, DOI: 10.1149/1.2407590.
49 T. T. Yang, R. B. Patil, J. R. McKone and W. A. Saidi, Revisiting trends in the exchange current for hydrogen evolution, *Catal. Sci. Technol.*, 2021, **11**(20), 6832–6838.
50 W. Du, E. H. Ang, Y. Yang, Y. Zhang, M. Ye and C. C. Li, Challenges in the material and structural design of zinc anode towards high-performance aqueous zinc-ion batteries, *Energy Environ. Sci.*, 2020, **13**(10), 3330–3360.
51 X. Guo and G. He, Opportunities and challenges of zinc anodes in rechargeable aqueous batteries, *J. Mater. Chem. A*, 2023, **11**(23), 11987–12001.
52 S.-B. Wang, Q. Ran, R.-Q. Yao, H. Shi, Z. Wen, M. Zhao, X.-Y. Lang and Q. Jiang, Lamella-nanostructured eutectic zinc–aluminum alloys as reversible and dendrite-free anodes for aqueous rechargeable batteries, *Nat. Commun.*, 2020, **11**(1), 1634, DOI: 10.1038/s41467-020-15478-4.
53 A. Chen, C. Zhao, J. Gao, Z. Guo, X. Lu, J. Zhang, Z. Liu, M. Wang, N. Liu and L. Fan, Multifunctional SEI-like structure coating stabilizing Zn anodes at a large current and capacity, *Energy Environ. Sci.*, 2023, **16**(1), 275–284.
54 D. Li, C. Li, W. Liu, H. Bu, X. Zhang, T. Li, J. Zhang, M. Kong, X. Wang and C. Wang, *et al.*, Constructing a Multifunctional SEI Layer Enhancing Kinetics and Stabilizing Zinc Metal Anode, *Adv. Funct. Mater.*, 2025, **35**(6), 2415107, DOI: 10.1002/adfm.202415107.

55 H. Wang, H. Li, Y. Tang, Z. Xu, K. Wang, Q. Li, B. He, Y. Liu, M. Ge and S. Chen, *et al.*, Stabilizing Zn Anode Interface by Simultaneously Manipulating the Thermodynamics of Zn Nucleation and Overpotential of Hydrogen Evolution, *Adv. Funct. Mater.*, 2022, **32**(48), 2207898, DOI: 10.1002/adfm.202207898.

56 X. Yu, M. Chen, Z. Li, X. Tan, H. Zhang, J. Wang, Y. Tang, J. Xu, W. Yin and Y. Yang, Unlocking dynamic solvation chemistry and hydrogen evolution mechanism in aqueous zinc batteries, *J. Am. Chem. Soc.*, 2024, **146**(25), 17103–17113.

